PAPER

Check for updates

Heterogenous Ni(OH)$_2$/NiOOH redox mediator on bismuth vanadate for photoelectrochemical oxidation of 5-hydroxymethylfurfural

Yuming Zhang (iD) * and Klaus Hellgardt (iD) *

Replacing the kinetically demanding O$_2$ evolution reaction (OER) in photoelectrochemical (PEC) water splitting with the anodic oxidation of biomass-derived 5-hydroxymethylfurfural (HMF) to 2,5-furandicarboxylic acid (FDCA), a key building-block chemical for polymer synthesis, offers a compelling strategy to improve both process efficiency and economic viability of solar–driven H$_2$ production. Although thermodynamically more favourable than the OER, direct HMF conversion is hindered by sluggish kinetics and high overpotential requirement, often necessitating redox mediators such as TEMPO to facilitate the conversion, which however introduces extra cost, process complexity and safety concerns. This study demonstrates that a Ni(OH)$_2$ nanoweb, electrodeposited on BiVO$_4$, functions as an effective solid-state redox mediator *via* photo-induced formation of NiOOH for PEC HMF oxidation. 48 hours of prolonged operation confirmed the formation of FDCA along with oxidation intermediates. Kinetic analysis revealed an apparent activation energy of 17.2 kJ mol^{-1} for HMF oxidation by NiOOH, significantly lower than that of conventional thermocatalytic processes. The Ni(OH)$_2$ coating also mitigated photocorrosion of BiVO$_4$, showing excellent stability of the heterostructured photoanode. These findings highlight the dual functionality of the electrodeposited Ni(OH)$_2$ as both a redox mediator for HMF oxidation and a protective layer for the photoelectrode, offering a stable and cost-effective alternative to existing PEC organic valorisation processes.

1. Introduction

With the advances in semiconductor technologies, photoelectrochemical (PEC) water splitting has emerged as a promising sustainable strategy to directly store solar energy in the form of chemical fuels. In a typical PEC system, the H$_2$ evolution reaction (HER) is performed at the cathode, coupled with the O$_2$ evolution reaction (OER) at the anode to complete the circuit. However, the OER is kinetically sluggish owing to its high overpotential requirement and yields O$_2$, which has limited economic value and poses additional safety concerns upon product crossover.[1–3] Therefore, replacing the OER with alternative anodic reactions that are both kinetically more favourable and produce value-added products can be beneficial to the efficiency and economic viability of PEC systems.

Among the various reactant candidates, 5-hydroxymethylfurfural (HMF) is an easily accessible, biomass-derived organic feedstock that can be oxidised to 2,5-furandicarboxylic acid (FDCA), an important precursor for bio-based polymer synthesis.[4,5] This conversion proceeds *via*

Department of Chemical Engineering, Imperial College London, London, SW7 2AZ, UK. E-mail: yuming.zhang20@imperial.ac.uk

a multi-step reaction pathway, as illustrated in Fig. 1, and is conventionally achieved through thermocatalytic aerobic oxidation involving the use of noble metal catalysts under elevated temperature and high-pressure O$_2$.[6] In contrast, PEC oxidation of HMF offers milder reaction conditions. It also has a lower thermodynamic barrier than the OER, potentially enabling the reaction to proceed with reduced energy input.[7,8]

Based on these concepts, Choi *et al.*[1] pioneered the PEC conversion of HMF to FDCA using 2,2,6,6-tetramethylpiperidine-1-oxy (TEMPO) as a redox mediator. In a BiVO$_4$ photoanode system, a near-quantitative FDCA yield and a faradaic efficiency (FE) of 93% were achieved. Building on these exciting results, surface modification of BiVO$_4$ with a co-catalyst such as Co–Pi[9] and, more recently, NiFe-LDH[10] has been demonstrated, reporting comparable FDCA yields with lower external potential required. In addition to BiVO$_4$, a wide variety of n-type semiconductors including Fe$_2$O$_3$ (ref. 11 and 12 and TiO$_2$ (ref. 13) have also been validated to effectively activate TEMPO, affording remarkable selectivity toward FDCA and high FE. All the studies above employed TEMPO, an established catalyst for alcohol and aldehyde oxidation, to scavenge the photogenerated holes from the surface of the photoanodes and mediate the transfer to the

602 | *Catal. Sci. Technol.*, 2026, **16**, 602–617

This journal is © The Royal Society of Chemistry 2026
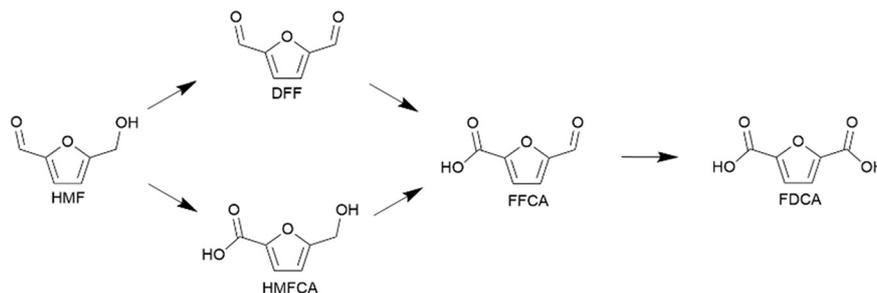
Fig. 1 Schematic illustration of the multi-step oxidation pathway from HMF to FDCA.

organic substrates. The presence of TEMPO also effectively suppresses the OER and thereby the formation of by-products by limiting the generation of ·OH radicals.[14] However, the practical application of TEMPO-mediated systems remains limited due to several inherent drawbacks including its extra cost, poor solubility in aqueous electrolytes, and genotoxicity to human cells.[15,16] The requirement for additional product separation steps increases the process cost and complexity. Moreover, TEMPO is found to be prone to degradation under prolonged operation, compromising long-term stability.[14,17] Direct oxidation of HMF on photoanodes has rarely been achieved due to the sluggish kinetics on the electrode.[1] Lhermitte et al.[17] demonstrated the unique ability of WO_3 to directly oxidise HMF. However, the FDCA yield remained below 1% after 60 hours, with HMF predominantly converted into by-products.

Direct HMF oxidation without a homogeneous redox mediator has been previously demonstrated in electrochemical systems using noble metal catalysts, such as Pt,[18] Ru[19] and Au–Pd alloy,[20] at the anode. More recently, efforts have shifted toward the development of earth-abundant alternatives, particularly Ni-based catalysts such as $Ni(OH)_2$,[21–24] owing to their reversible and electroactive redox transition between Ni^{2+} and Ni^{3+}. Among the proposed mechanisms,[25,26] the latter in the form of NiOOH is widely recognised for its high catalytic activity toward HMF oxidation and its potential to act as a heterostructured redox mediator at the electrode surface. Although this $Ni(OH)_2$/NiOOH redox couple has not been explored in a PEC HMF oxidation system, largely due to a prevailing assumption that NiOOH, a well-established OER catalyst on photoanodes, would favour the competing OER over the desired HMF oxidation,[1] surface modification of $BiVO_4$ photoanodes has been widely investigated as an effective strategy to regulate interfacial charge transfer and improve product selectivity. Recent work employing a SnO_2 overlayer on $BiVO_4$ demonstrated that such surface modification can suppress the OER by steering the hole transfer path, thereby enhancing the selectivity toward the desired water oxidation to H_2O_2, which subsequently facilitated propylene epoxidation.[27,28] Building on the established oxidative reactivity of NiOOH toward HMF in electrocatalytic systems as well as the effect of surface modification on the electrode

kinetics, it was hypothesised that integrating $Ni(OH)_2$ with photoanodes to form a heterostructured photoelectrode could enable its transformation to NiOOH by the photogenerated holes in a PEC setting. The resulting NiOOH would subsequently oxidise HMF at the electrode–electrolyte interface to form FDCA while being reduced back to $Ni(OH)_2$, as illustrated in Fig. 2.

In the present work, the long-term stability of a typical TEMPO-mediated PEC system was first evaluated. The redox activity of the $Ni(OH)_2$/NiOOH couple and its catalytic reactivity toward HMF oxidation were investigated. An indirect electrodeposition approach was then developed and optimised to synthesise a conformal $Ni(OH)_2$ nanoweb on $BiVO_4$, an n-type semiconductor selected based on its adequate stability and suitable band alignment. Prolonged PEC operation with the proposed system was later performed to demonstrate the viability of the proposed $Ni(OH)_2$/NiOOH-mediated HMF oxidation, followed by detailed product analysis. Furthermore, kinetic studies were carried out by independently varying the substrate concentration, temperature, and electrolyte flow rate to identify the rate-limiting step and determine the activation energy. Lastly, the electrochemical and structural stability of the heterostructured photoelectrode was examined through
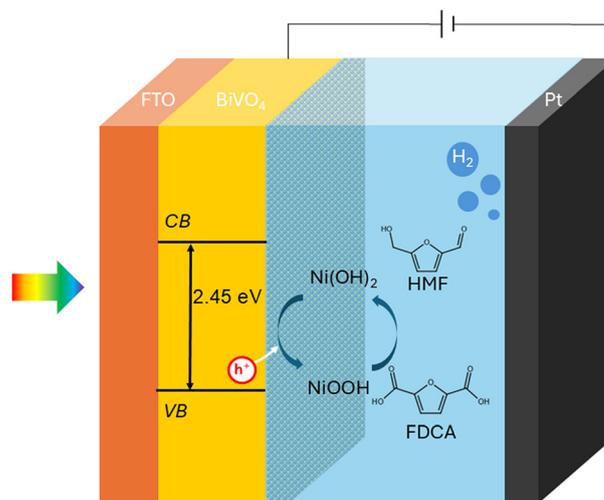

Fig. 2 Schematic illustration of the PEC system for HMF oxidation mediated by the $Ni(OH)_2$/NiOOH redox couple.

This journal is © The Royal Society of Chemistry 2026

Catal. Sci. Technol., 2026, **16**, 602–617 | **603**

repeated cycling tests and post-reaction material characterisation.

2. Experimental section

2.1. Materials

The following chemicals were used as received without further purification. VO(acac)$_2$ (98%), Bi(NO$_3$)$_3$·5H$_2$O (98%), HNO$_3$ (69%), DMSO (99.5%), H$_3$BO$_3$ (≥99.5%), Ni(NO$_3$)$_2$·6H$_2$-O (≥98.5%), Na$_2$SO$_3$ (≥98) and fluorine-doped tin oxide-coated glass slides (FTO, surface resistivity ~8 Ω sq^{-1}) were purchased from Sigma-Aldrich. HMF (98%) and KI (≥99.5%) were purchased from Fisher Scientific. Absolute ethanol (99.8%) and 1,4-benzoquinone (99%) were purchased from Thermo Scientific. FDCA (98%) and TEMPO (≥98%) were purchased from Alfa Aesar. DFF (95%), HMFCA (95%) and FFCA (98%) were purchased from Fluorochem. NaOH (≥98.5%) and KCl (99.5%) were purchased from VWR International. Deionised water (DI, ≤18 MΩ cm) was used to prepare aqueous solutions.

2.2. Preparation of BiVO$_4$ photoelectrodes

BiVO$_4$ photoelectrodes were synthesised by adopting a previously reported two-step method with modifications.[29] 50 mL of aqueous solution A containing 0.4 M KI and 0.04 M Bi (NO$_3$)$_3$ was prepared. The pH of the solution was adjusted to 1.67 by adding concentrated HNO$_3$ prior to the addition of the bismuth source to ensure complete ionisation of Bi^{3+}. Solution B was prepared by dispersing 0.23 M 1,4-benzoquinone in 20 mL of ethanol. The electroplating solution was completed by mixing solution B into solution A dropwise under vigorous stirring to prevent premature precipitation. A three-electrode setup consisting of a fluorine-doped tin oxide (FTO)-coated glass working electrode, a Pt plate (10 mm × 10 mm) counter electrode and an Ag/AgCl reference electrode was used for electrodeposition. The Ag/AgCl electrode (purchased from Beijing Jingke) was filled with 3 M KCl solution upon receipt and stored in the same solution when not in use. Conversion between the potentials versus the reference electrode and the reversible hydrogen electrode (RHE) refer to eqn (1) and (2).

$$E(vs.\ \text{RHE}) = E(vs.\ \text{Ag/AgCl}) + E^0_{\text{Ag/AgCl}} + \text{pH} \times 0.0591\ \text{V} \quad (1)$$

$$E^0_{\text{Ag/AgCl}} = 0.210\ \text{V}\ vs.\ \text{NHE at 25 °C for 3 M KCL} \quad (2)$$

The FTO-coated glass substrates were ultrasonically cleaned with deionised (DI) water and isopropanol before masking the active area (14 mm × 14 mm) using Kapton tape. The BiOI precursor was electrodeposited on FTO substrates at a constant potential of −0.1 V vs. Ag/AgCl for 5 minutes using an EZstat-pro potentiostat. 200 μL of DMSO solution containing 0.2 M VO(acac)$_2$ was subsequently drop-cast onto each BiOI-coated sample followed by annealing at 450 °C for 2 hours (ramp rate of 2 °C min^{-1}) in a muffle furnace. Excess V$_2$O$_5$ was removed by soaking the resulting samples in 1 M NaOH for 30 minutes under gentle stirring to obtain the pristine BiVO$_4$ photoelectrodes.

2.3. Synthesis of Ni(OH)$_2$ on FTO and BiVO$_4$

A similar three-electrode configuration was employed to electrochemically deposit Ni(OH)$_2$ on FTO substrates. The aqueous electroplating solution contained 10 mM Ni(NO$_3$)$_2$ and the pH was adjusted to fall within the range of 7 ± 0.2 by adding either diluted HNO$_3$ or NaOH. The plating solution was purged with N$_2$ for 30 minutes and stored in a sealed container before use. Cathodic deposition was conducted potentiostatically at −0.7 V vs. Ag/AgCl for durations ranging from 5 to 20 minutes. The as-prepared samples were rinsed with DI water and dried with N$_2$.

In order to synthesise Ni(OH)$_2$ on BiVO$_4$ electrodes, the same procedure was followed except that the FTO substrates were replaced with BiVO$_4$-coated samples as the working electrode. The electrochemical cell was purposely kept in the dark during deposition to avoid side reactions resulting from the photogenerated electrons.

2.4. Material characterisation

The crystal structure and the compositional purity of the Ni(OH)$_2$ film were examined using the X-ray diffraction (XRD) patterns obtained with a PANalytical Empyrean diffractometer equipped with a Cu anode and a binary Kα source ($\lambda_{\text{K}\alpha1}$ = 1.5406 Å and $\lambda_{\text{K}\alpha2}$ = 1.5444 Å) operated at 40 kV and 40 mA. To observe the surface and the cross-sectional morphologies of the electrodes, scanning electron microscopy (SEM) was performed using a Zeiss Gemini Sigma-300 microscope with the accelerating voltage of the field emission gun set at 5 kV. All samples for SEM imaging were coated in advance with a 15 nm thick Cr film using a Q150T Quorum sputter coater to increase the surface conductivity. XPS analyses were performed to investigate the elemental composition, bonding environment and the oxidation state of the electrodes. Measurements were carried out suing a Thermo Fisher K-Alpha+ spectrometer equipped with a monochromatic Al Kα radiation source. The instrument base pressure was maintained below 8 × 10^{-8} mbar during the spectra collection. Pass energy was set to 20 eV when collecting high-resolution spectra. The binding energies were calibrated with respect to the C 1s peak at 284.8 eV.

2.5. Electrochemical and photoelectrochemical measurements

All electrochemical and PEC measurements were controlled using the EZstat-pro potentiostat in a standard three-electrode configuration, with the prepared electrode (specified individually) as the working electrode, a Pt plate as the counter electrode and an Ag/AgCl (3 M KCl) electrode as the reference electrode. The borate buffer used in this study refers to the aqueous solution containing 0.5 M H$_3$BO$_3$ and approximately 0.2 M NaOH to adjust pH to 9.2. Such

604 | Catal. Sci. Technol., 2026, **16**, 602–617

This journal is © The Royal Society of Chemistry 2026

conditions were selected since it is considered the most suitable long-term operation,[30] as BiVO$_4$ undergoes photocorrosion and chemical etching in strongly acidic and alkaline medium. Active species of HMF (5 mM, 50 mM, 100 mM), DFF (5 mM), FFCA (5 mM), and TEMPO (7.5 mM) were added to the electrolyte for specific studies. All electrolytes were purged with N$_2$ for 30 minutes prior to any electrochemical analyses and prolonged operations. A customised undivided cell that was suitable for both electrochemical and PEC applications was implemented. The working electrode was embedded in the cell, forming part of the cell wall. The opposite wall was made of quartz to allow for *in situ* optical measurements. The active working electrode area was 0.79 cm^2; all reported current densities were normalised to this area in this study. The counter and the reference electrodes were inserted into the electrolyte and kept at fixed positions for consistent ion path length in the bulk solution.

An Abet Technologies Sun-2000 solar simulator equipped with an AM 1.5 G filter was used to provide the irradiation required for PEC analyses. The working electrode was back-illuminated, and the incident light intensity reaching the surface of the electrode (before penetrating the FTO substrate) was calibrated to 100 mW cm^{-2} (equivalent to 1 sun) using an International Light Technologies ILT-1400 photometer. To monitor the *in situ* optical changes and assess the reversibility of the Ni(OH)$_2$/NiOOH redox couple, a UV-visible spectroscopic setup was assembled by placing a B&W TEK BWS-005 spectrometer behind the quartz window to capture the light transmittance through the cell. The data presented were normalised and converted to absorbance according to the Beer–Lambert law.

Linear sweep voltammetry (LSV) and cyclic voltammetry (CV) scans were performed at scan rates of 10 mV s^{-1} and 20 mV s^{-1}, respectively, starting with a positive direction unless specified otherwise. For all CV scans, at least three cycles were collected and the results shown correspond to the third cycle. To ensure a uniform initial oxidation state of the Ni(OH)$_2$ electrodes, two preparatory CV scans were conducted at the start of each measurement. For prolonged PEC reactions, the cell was filled with 12 mL electrolyte, and a constant potential of 0.3 V *vs.* Ag/AgCl (1.05 V *vs.* RHE) was applied for 48 hours.

2.6. Product quantification

During the prolonged PEC reactions, 100 μL of electrolyte samples were withdrawn from the cell at regular intervals. Samples were diluted to 1 mL with DI water prior to being analysed using a Shimadzu LC-2030C high-performance liquid chromatography (HPLC) instrument. The detector unit was a diode array detector (DAD) set at a monochromatic wavelength of 265 nm. The separation was achieved using a 300 mm × 7.8 mm Supelcogel C610H column. The mobile phase consisted of 6 mM H$_2$SO$_4$, run at a flow rate of 0.5 mL min^{-1}. The column temperature was maintained at 55 °C,

and the injection volume was 10 μL. The identification and quantification were obtained from calibrated curves prepared by running standard samples of known concentrations. HMF conversion, oxidation product yield and FE were calculated following eqn (3)–(5).

$$\text{Conversion (\%)} = \frac{\text{mol of consumed HMF}}{\text{mol of initial HMF}} \times 100\% \quad (3)$$

$$\text{Yield (\%)} = \frac{\text{mol of product}}{\text{mol of initial HMF}} \times 100\% \quad (4)$$

$$\text{FE}_{\text{product}} \text{ (\%)} = \frac{\text{mol of products} \cdot n \cdot F}{Q_{\text{Total}}} \times 100\% \quad (5)$$

where n is the number of electrons involved in the reaction (*e.g.*, 2 for HMF oxidation to DFF and 6 for HMF oxidation to FDCA) and F is Faraday's constant. The total FE was defined as the sum of efficiencies calculated for each identifiable HMF-derived product.

A Shimadzu ISR-2600 Plus spectrophotometer was employed as a supplement to identify the absorption wavelengths as well as to quantify TEMPO in the electrolyte. The absorbance spectra of TEMPO were recorded within the range of 350–550 nm and the baseline was corrected by using borate buffer as the reference solution. Calibration curves were constructed by adding TEMPO into borate buffer at various concentrations.

2.7. Kinetic studies

Kinetic studies were conducted in a custom-designed undivided PEC flow cell, allowing for flow rate variation and external temperature control. The system setup and electrode configuration were identical to those used for batch reactions, except that the Pt plate counter electrode was replaced by a Ni sheet, and the size of the working electrode was enlarged to 1.96 cm^2. The counter electrode also formed part of the cell wall alongside the working electrode, instead of being immersed in the electrolyte, creating an unbaffled laminar flow chamber. The electrolyte leaving from the outlet (at the top of the flow chamber) was recirculated to the inlet (bottom), passing through a 50 mL electrolyte reservoir. Electrolyte flow was driven by a peristaltic pump. Temperature control was achieved by soaking the reservoir in a water bath. PVC tubing was wrapped in aluminium foil when necessary to minimise heat loss, enabling more accurate thermal operation. To investigate the effect of temperature on the reaction rate, current densities were monitored after establishing steady operation for 15 minutes at 1.05 V *vs.* RHE. The current densities reported represent average values recorded over a duration of 20 seconds. The activation energy was determined using the Arrhenius equation.

3. Results and discussion

3.1. Evaluation of homogeneous redox mediators for HMF oxidation

The oxidation reactions of HMF and its oxidation intermediates (*i.e.*, DFF, HMFCA and FFCA) have lower reduction potentials than that of the competing OER. This suggests that HMF oxidation is thermodynamically more favourable on the photoanode, and lower bias is required to activate the reaction. To assess the necessity of adding redox mediators and the effectiveness of TEMPO in catalysing HMF oxidation, voltametric analyses were performed in borate buffer (pH 9.2) with and without the addition of HMF and TEMPO (Fig. 3). From the linear sweep voltammetry (LSV) of the electrolyte containing neither HMF nor TEMPO, a clear onset potential was observed at 0.5 V *vs.* RHE, and the photocurrent steadily increased with the applied potential. This behaviour in consistent with previously reported OER characteristics on the BiVO$_4$ photoanode.[29] Upon the addition of 5 mM HMF into the electrolyte, the onset potential did not shift significantly, indicating that the OER was still the dominant reaction. Moreover, the photocurrent that responded to the increasing potential was lower in magnitude than that without the presence of HMF. This result contradicts the expectation that the HMF oxidation would have a lower thermodynamic barrier than the OER. Such divergence was presumably due to competitive adsorption between the OH$^-$ ions and the hydroxyl groups of HMF on the anode surface, which is considered crucial for catalytic OER and alcohol oxidation.[7,31] The adsorbed HMF molecules could not be readily oxidised owing to the high overpotential required, resulting in a blockage of binding sites for OH$^-$ ions and suppressing the rate of the OER. A 48 hour prolonged reaction was carried out at a constant applied potential of 1.05 V *vs.* RHE. Only 2.8% HMF conversion was observed, accompanied by negligible formation of oxidation products (SI Fig. S1), indicating a minimal activity of HMF on the surface of bare BiVO$_4$.

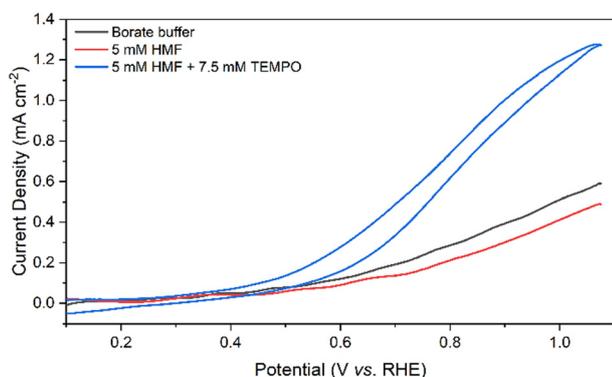Following the combined introduction of 7.5 mM TEMPO and 5 mM HMF, cyclic voltammetry (CV) revealed a negative

shift of onset potential by 0.4 V and a remarkable enhancement of the photocurrent compared to HMF alone. The high photocurrent was attributed to the oxidation of TEMPO to TEMPO$^+$ cations by the photogenerated holes and the simultaneous regeneration while receiving electrons from the organic species.[1] The regenerated TEMPO molecules reinforced the PEC reaction at the electrode surface. These results confirm the enhanced PEC activity of TEMPO on the electrode surface as well as the subsequent oxidation of HMF by the TEMPO$^+$ cations. Additionally, no cathodic peak was detected during the reverse CV scan, suggesting rapid consumption of TEMPO$^+$ *via* fast reaction with HMF.

To evaluate the efficacy of producing desired oxidation products and the stability of TEMPO as a redox mediator, prolonged PEC reaction was carried out in a custom-built flow cell by applying a constant potential of 1.05 V *vs.* RHE. 50 mL borate electrolyte solution (pH 9.2) containing 5 mM HMF and 7.5 mM TEMPO was circulated through the reactor chamber at a flow rate of 3 mL min^{-1} in order to minimise pH and concentration gradient build-up.[32,33] In view of the ohmic resistance, instability and the cost associated with commercial anion exchange membranes,[34] the flow cell used in this study adopted a membrane-free undivided configuration. Product crossover and the cathodic reduction of the oxidation products could be effectively alleviated by establishing laminar flow between the parallel electrodes.[35] The electrolyte samples were regularly taken and analysed using HPLC throughout the 48 hour PEC operation, and the evolution of product composition is shown in Fig. 4a. At the initial stage of the reaction, HMF was primarily oxidised into DFF and no formation of HMFCA was detected. This shows agreement with the widely recognised mechanism in which the hydroxyl group on HMF is more susceptible to oxidation than the aldehyde group at pH <13.[36,37] Correspondingly, the formation rate of FDCA was limited by the slow oxidation of aldehyde groups, and a considerable amount of FFCA remained at the later stage. After 48 hours of reaction, the HMF conversion and the yield of FDCA reached 98.8% and 63.4%, respectively. Nevertheless, the total FE, calculated based on all identifiable products, remained as low as 57.3%. In addition to the known factors such as the competing OER and potential reduction of some oxidation products at the cathode, it was postulated that the decomposition of the oxoammonium cations, formed from oxidised TEMPO, *via* over-oxidation also contributed to the low FE.[38]

The transformation of TEMPO was investigated by performing UV-vis spectroscopy on the electrolyte collected after the reaction. Fig. 4b compares the sample spectra of the post-reaction electrolyte with standard TEMPO (max. abs 425–435 nm)[39] spectrum of various concentrations. The absorbance in the lower-wavelength region (<425 nm), resulting from the oxidation products such as FDCA and FFCA, was normalised using a reference solution prepared with the same product composition as determined by the HPLC results (see SI Fig. S2 for detailed normalisation). A TEMPO concentration of 7.5 mM, representing the pristine

Fig. 3 Photocurrents of BiVO$_4$ photoanodes. LSV and CV with electrolyte with and without 5 mM HMF and 7.5 mM TEMPO. Scan rate = 10 mV s^{-1}.
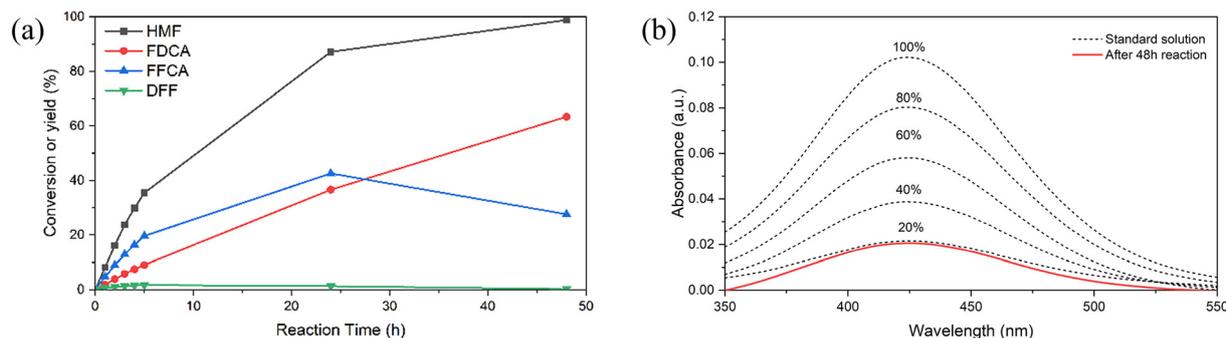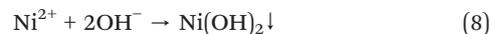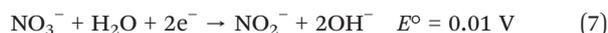
Fig. 4 Product analyses of a 48 hour TEMPO-mediated PEC reaction. (a) HMF conversion (started with 5 mM) and yields of the oxidation products. (b) Normalised UV-vis spectrum of post-reaction electrolyte compared to standard TEMPO solutions (100% represents 7.5 mM at the start of the reaction).

electrolyte before the reaction, is denoted as 100%. After the 48 hour reaction, a reduction of over 80% in TEMPO concentration was observed. While the absorbance decay and associated loss of FE can result from decomposition of over-oxidised oxoammonium cations, it may also reflect the inevitable disproportion of TEMPO during the catalytic reaction, yielding the hydroxylamine species TEMPOH, which exhibits negligible absorbance within the tested UV-vis range.[40] TEMPOH remains inert even upon the presence of O_2; the reactivation of TEMPOH generally necessitates the addition of a strong oxidant such as NO_2^-, which brings about additional processing complexity.[40]

This finding raises concerns about the long-term stability of TEMPO as a redox mediator in PEC applications. Combining other limitations, particularly the low solubility of TEMPO in aqueous solution, it appears unsuitable for up-scaled PEC systems. Identifying a more suitable alternative would therefore be conducive to improving the process efficiency.

3.2. Synthesis and characterisation of Ni(OH)$_2$

The Ni-based redox mediator can be constructed on an electrode *via* the electrodeposition of either NiOOH or Ni(OH)$_2$ from a Ni^{2+}-containing plating solution. NiOOH is typically obtained by electrochemically oxidising Ni^{2+} to a transient ion of Ni^{3+}, which subsequently precipitates in the form of solid NiOOH by coordinating with OH^- ions.[41] However, this conversion requires high overpotentials, and the metastability upon air exposure gives rise to difficulties for storage and *ex situ* characterisation.[42] On the other hand, Ni(OH)$_2$ is usually produced through an indirect method that electrochemically raises the local pH at the electrode surface.[43–45] The most common reactions involve the reduction of water (eqn (6)) or NO^{3-} (eqn (7)), which increases the local concentration of OH^-, thereby leading to the nucleation of Ni(OH)$_2$ (eqn (8)).

$$H_2O + 2e^- \rightarrow H_2 + 2OH^- \quad E^\circ = -0.83 \text{ V} \tag{6}$$

$$NO_3^- + H_2O + 2e^- \rightarrow NO_2^- + 2OH^- \quad E^\circ = 0.01 \text{ V} \tag{7}$$

$$Ni^{2+} + 2OH^- \rightarrow Ni(OH)_2\downarrow \tag{8}$$

Due to the less restrictive requirements for the characterisation techniques and improved control over film morphology, the synthesis of Ni(OH)$_2$ is deemed more practical and was therefore employed in this study. Ni(OH)$_2$ was electrodeposited under potentiostatic conditions at −0.7 V *vs.* Ag/AgCl (−0.077 V *vs.* RHE). This applied potential was determined from a control experiment (SI Fig. S3) to ensure that Ni^{2+} reduction does not occur concurrently. In addition to the deposition potential, the pH of the plating solution was also found to play a critical role in current densities, hence the rate of Ni(OH)$_2$ formation. To ensure reproducibility, a near-neutral condition (pH = 7 ± 0.2) was maintained in this study, as it resulted in a moderate deposition rate that affords better control over film thickness and surface morphology.

Ni(OH)$_2$ was first synthesised on FTO substrate for corroborative examination of its physical properties and its redox activity. SI Fig. S4 presents SEM images confirming the formation of uniform and continuous Ni(OH)$_2$ nanofibres on FTO. Following a 10 minute electrodeposition, XRD showed no perceptible diffraction peaks from the FTO substrate (SI Fig. S5). This is presumably attributable to the formation of the amorphous α-Ni(OH)$_2$, which exhibits higher surface reactivity and superior electrocatalytic performance compared to its more crystalline β-form counterpart.[46–48] XPS was performed to further substantiate the formation of the Ni(OH)$_2$ coating, and the binding energy spectra are presented in Fig. 5. Fig. 5a displays the spectrum of Ni 2p, where the deconvoluted components were fitted with two pairs of doublets and two individual satellite peaks. The main peaks at 855.4 eV (Ni 2p$_{3/2}$) and 573.1 eV (Ni 2p$_{1/2}$) show strong agreement to the commonly reported binding energies for Ni(OH)$_2$.[49,50] Two additional shoulder peaks at 857.0 eV and 874.9 eV were designated to Ni^{3+}, which is often found coexisting with Ni^{2+} in the synthesised Ni(OH)$_2$ samples.[46,48,51] This is due to the presence of Ni vacancies on the electrode surface[52] resulting from the excess amount of OH^- ions generated during the indirect electrodeposition and a local deficit of Ni^{2+} that reinforces the formation of

This journal is © The Royal Society of Chemistry 2026

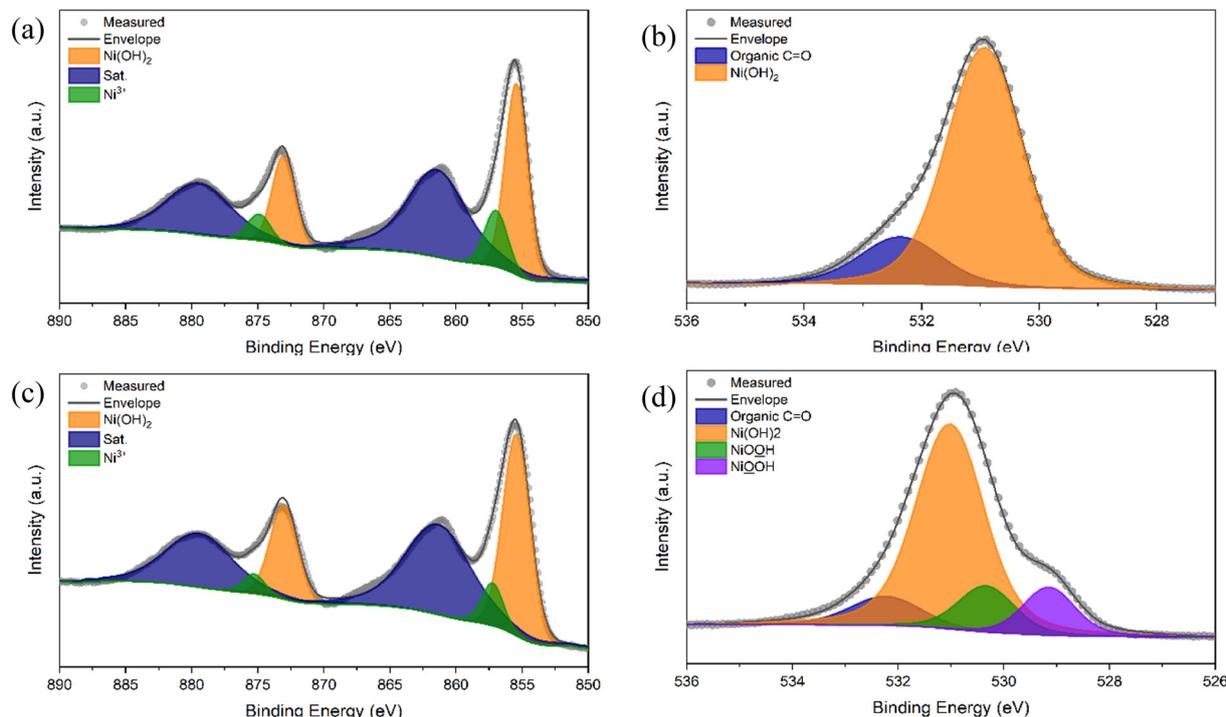*Catal. Sci. Technol.*, 2026, **16**, 602–617 | **607**

Fig. 5 XPS spectra of the fitted (a) Ni 2p and (b) O 1s regions obtained from the electrodeposited Ni(OH)$_2$ coating and the corresponding (c) Ni 2p and (d) O 1s regions of the electrochemically oxidised NiOOH sample, including the deconvoluted components. The NiOOH sample was prepared by anodic oxidation of the Ni(OH)$_2$ coating at 1.49 V vs. RHE for 1 minute.

Ni(OH)$_2$. The absence of an elemental Ni peak (typically around 852.6 eV) provides additional validation of the selected electrodeposition potential. To further verify the coating composition, the O 1s spectrum was also obtained and is displayed in Fig. 5b. Apart from the 532.1 eV peak assigned to the organic contaminations, a solitary peak at 530.7 eV supports the compositional uniformity of the Ni(OH)$_2$ film.[50]

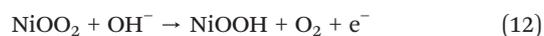### 3.3. Electrochemical redox behaviour of Ni(OH)$_2$/NiOOH

To examine the electrochemical redox activity of the as-prepared Ni(OH)$_2$ coating, a CV scan was conducted in 1 M KOH solution using a custom-designed cell where *in situ* UV-vis spectra were collected synchronously. As demonstrated by the CV analysis (black line) in Fig. 6a, two nearly symmetric peaks were obtained at 1.41 (peak A) and 1.31 V vs. RHE (peak D) for anodic and cathodic scans, respectively. These two peaks correspond to electrochemically reversible oxidation state transition of Ni^{2+}/Ni^{3+} in the form of Ni(OH)$_2$ and NiOOH (eqn (9)).

$$\text{Ni(OH)}_2 + \text{OH}^- \leftrightarrow \text{NiOOH} + \text{H}_2\text{O} + \text{e}^- \quad E^\circ = 1.40 \text{ V} \quad (9)$$
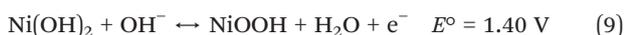
A second oxidation peak (peak B) was observed at 1.56 V vs. RHE, indicative of the phase transition from β-Ni(OH)$_2$ to β-NiOOH.[53,54] This suggests a mixed-phase composition of the electrodeposited coating, with a relatively smaller proportion of β-Ni(OH)$_2$ present. Integration of the oxidation

and reduction peaks shows that the overall charge of peak D is closely equivalent to the summation of peaks A and B, lending further support to the described phase transition.

As the applied potential increases, the Ni species undergo transitions to higher oxidation states, such as Ni^{4+} and Ni^{6+}, which subsequently catalyse the OER. The exact mechanism of electrocatalytic OER on Ni is known to depend on factors such as the supporting electrolyte and pH conditions.[26] Based on the obtained CV pattern, the transition mechanism is deduced to follow a widely accepted sequence proposed in previous studies (eqn (10)–(12)).[21,26]

$$\text{NiOOH} + \text{OH}^- \leftrightarrow \text{NiO(OH)}_2 + 2\text{e}^- \quad (10)$$

$$\text{NiO(OH)}_2 + 2\text{OH}^- \leftrightarrow \text{NiOO}_2 + 2\text{H}_2\text{O} + 2\text{e}^- \quad (11)$$

$$\text{NiOO}_2 + \text{OH}^- \rightarrow \text{NiOOH} + \text{O}_2 + \text{e}^- \quad (12)$$

At higher potentials, NiOOH is initially oxidised to a hydrous Ni oxide (NiO(OH)$_2$) (eqn (10)) and sequentially undergoes further reconstruction to form Ni peroxide (NiOO$_2$) (eqn (11)), which then facilitates the formation of O$_2$ through an anodic reduction process back to NiOOH (eqn (12)). This reaction is kinetically fast and irreversible, leading to a sharp current spike beyond 1.6 V vs. RHE (denoted as C). Moreover, no corresponding cathodic peak was observed, suggesting a complete regeneration of NiOOH.

The electrochemical transition between Ni(OH)$_2$ and NiOOH is accompanied by a distinct optical change due to
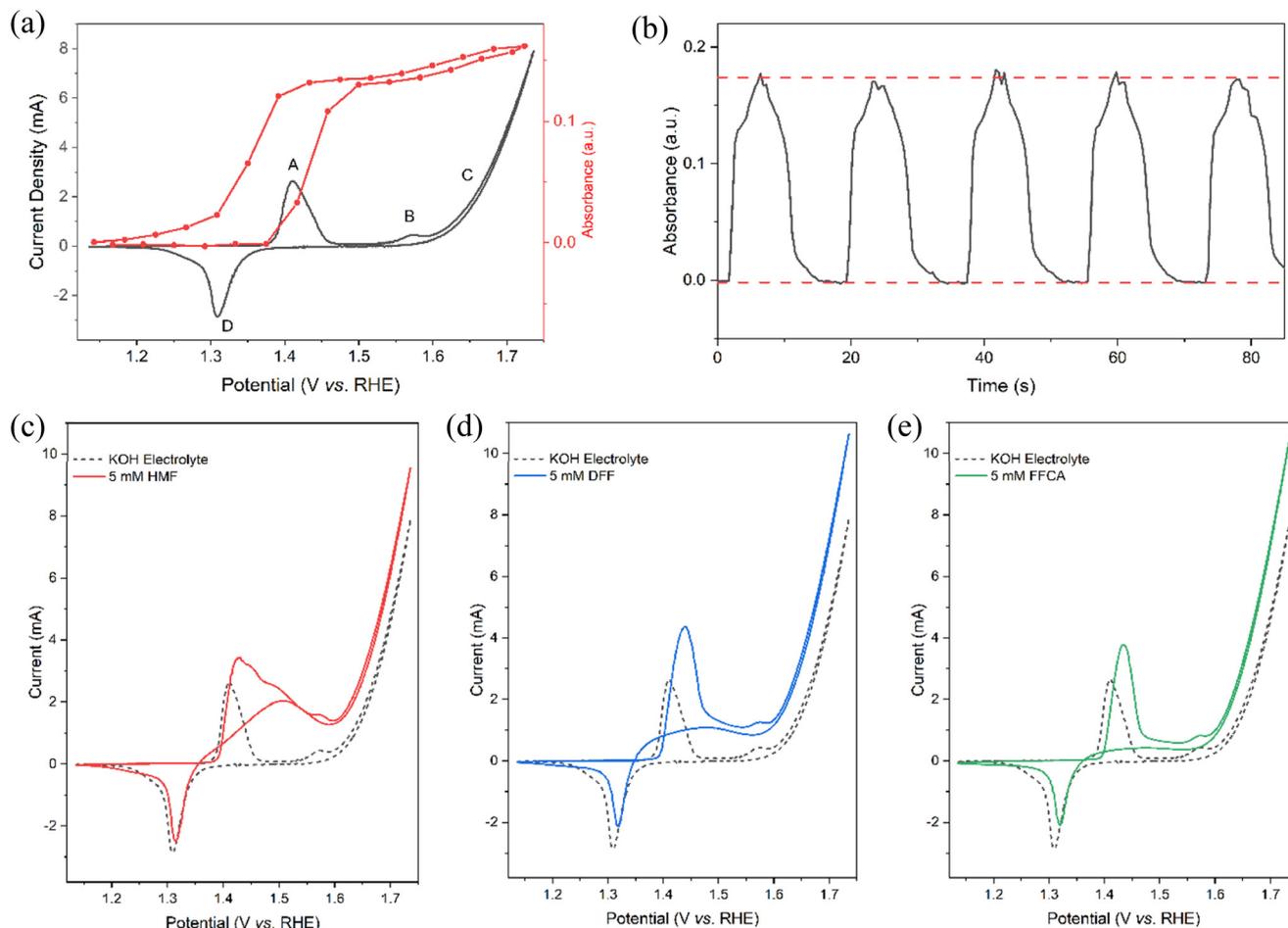
608 | *Catal. Sci. Technol.*, 2026, **16**, 602–617

This journal is © The Royal Society of Chemistry 2026

Fig. 6 Electrochemical redox characteristics of electrodeposited Ni(OH)$_2$. (a) Overlay of the synchronous CV scan and the corresponding *in situ* UV-vis profile (λ = 570 nm) measured in 1 M KOH. (b) Absorbance profile recorded over the last 5 cycles of an extended 20-cycle CV measurement. CV measurements recorded with (coloured) and without (black) the addition of 5 mM (c) HMF, (d) DFF, and (e) FFCA. Scan rate = 20 mV s^{-1}.

their different UV-vis absorption characteristics. Ni(OH)$_2$ absorbs primarily in the UV region and appears visually transparent in thin films, whereas NiOOH exhibits visible light absorption, with wavelength centred around 590–620 nm.[54] As a result, the electrode surface turns dark upon the formation of NiOOH. *In situ* UV-vis spectroscopy was employed to monitor changes in Ni oxidation states and the coordination environment, and the absorbance profiles at 570 nm are demonstrated in Fig. 6a and b. As shown in Fig. 6a (red line), the absorbance begins to rise at ~1.4 V *vs.* RHE, which is in line with the onset of NiOOH formation and the corresponding colouration. A brief plateau was reached between 1.5 and 1.6 V *vs.* RHE owing to the depletion of Ni(OH)$_2$. Beyond this point, the absorbance increases further due to the evolution of visually apparent O$_2$ bubbles on the electrode surface, which partially scatter the incident light. During the backward scan, an inverse absorbance decline starting from 1.4 V *vs.* RHE was also found to be correlated with the cathodic regeneration of Ni(OH)$_2$, and it eventually returned to the starting point as the current offset. The stability and reproducibility of the redox couple was further assessed by extending the CV

measurement for an additional 20 cycles, with the *in situ* absorbance profiles of the last 5 cycles exemplified in Fig. 6b. A well-defined and stable periodicity with reasonably consistent absorbance peak and trough values are illustrated by the dotted line (in red), indicating good cycling stability and reversibility of the Ni(OH)$_2$/NiOOH redox couple. The secondary absorbance increases, observed as shoulder features during the colouration step, were also found synchronous with the O$_2$ evolution (peak C) in Fig. 6a.

To provide evidence for the formation of NiOOH by electrochemical oxidation of Ni(OH)$_2$, *ex situ* XPS spectra of Ni 2p (Fig. 5c) and O 1s (Fig. 5d) were obtained following potentiostatically oxidising Ni(OH)$_2$ coating at 1.49 V *vs.* RHE for 1 minute. Although a Ni^{3+} peak at 857.0 eV was deconvoluted in the Ni 2p spectrum, the main peak at 855.4 eV, which is typically associated with the binding energy of Ni^{2+} in Ni(OH)$_2$, remained dominant. The overall spectral profile showed no substantial difference from the spectrum obtained for Ni(OH)$_2$ (Fig. 5a). Therefore, the Ni 2p spectrum alone appears inadequate for reliably distinguishing the redox transition between Ni(OH)$_2$ and NiOOH.[55] In contrast, the O 1s spectrum discloses intriguing components with

This journal is © The Royal Society of Chemistry 2026

Catal. Sci. Technol., 2026, **16**, 602–617 | **609**

lower binding energies than $Ni(OH)_2$ (530.7 eV), which are uniquely present in the NiOOH sample when compared with $Ni(OH)_2$ (Fig. 5b). Due to the metastable nature of NiOOH, the exact interpretation of the O 1s characteristics of the *ex situ* XPS remains ambiguous. While some researchers report a single O 1s peak above 530 eV for NiOOH,[51,56] the results of this study clearly support the perspective that NiOOH gives rise to two separate peaks with lower binding energies, attributed to O^{2-} and OH^-, respectively.[50,57] Accordingly, the additional shoulder features in the O 1s spectrum were fitted with two peaks at 530.4 and 529.1 eV. The area ratio of these two peaks was constrained to 1.0 ± 0.1, assuming ideal stoichiometry of NiOOH. The dominant signal at 530.7 eV was nevertheless ascribed to $Ni(OH)_2$, confirming that the spontaneous reduction of NiOOH indeed occurs readily upon exposure to water or air.[50]

Another important preliminary evaluation before employing the redox mediator in the targeted organic oxidation reaction is to confirm the chemical reactivity between the electrochemically produced NiOOH and HMF along with other relevant intermediates. Accordingly, CV measurements were performed in 1 M KOH in the absence and presence of 5 mM of each organic species (Fig. 6c–e). Fig. 6c illustrates the influence on the current profile upon the addition of HMF. An increase in anodic current was observed during the forward scan, attributed to the concurrent regeneration of $Ni(OH)_2$ *via* chemical oxidation of HMF, which reinforces the electrochemical reaction. As a result, additional charge was required to fully convert $Ni(OH)_2$ to NiOOH. Conversely, a diminished cathodic current was recorded during the reverse scan, as a fraction of the NiOOH had been chemically reduced back to $Ni(OH)_2$ prior to the onset of the electrochemical reduction. It is also noted that during the forward scan, the onset of the anodic current shifted slightly (~0.01 V) toward a more positive potential. This is due to the adsorption of HMF onto Ni^{2+} sites, introducing further thermodynamic barriers to the electrochemical oxidation.[22] The β-$Ni(OH)_2$ transition also appears as a second anodic peak at 1.56 V *vs.* RHE, although the magnitude enhancement in response to HMF is less pronounced than that of the first anodic peak, indicating a higher electrocatalytic activity with the α-phase than the β-phase. Once the potential was swept beyond 1.6 V *vs.* RHE, the formation of Ni^{4+} and Ni^{6+} led to the OER becoming the prevailing factor contributing to the current rise. This suggests that although Ni sites may still retain oxidative activity toward HMF, the adsorption of HMF on Ni sites is substantially less favourable relative to OH^-, particularly under high pH conditions.[25] Furthermore, a broad anodic wave was observed during the reverse scan, which is superficially atypical in CV measurements. This insightful feature reflects the continuing chemical oxidation of HMF by NiOOH during the CV scan, and the anodic current during the reverse scan results from the re-oxidation of the chemically reduced $Ni(OH)_2$.

For a complete oxidation path from HMF to FDCA, it is essential to ascertain the reactivity of NiOOH toward other oxidation intermediates. Based on the previously discussed reaction sequence under moderately alkaline conditions, NiOOH must also exhibit oxidative activity toward DFF and FFCA. Accordingly, analogous CV analyses were conducted in the presence of each intermediate. As shown in Fig. 6d and e, the CV features for DFF and FFCA closely resemble those observed for HMF, which are attributable to the same redox mechanism discussed above. This supports the conclusion that the $Ni(OH)_2$/NiOOH redox couple is capable of driving the complete oxidation of HMF to FDCA. A notable distinction, however, is a secondary current between 1.45 and 1.55 V *vs.* RHE in the anodic profile of HMF. In contrast, the anodic currents associated with DFF and FFCA appear as well-defined and stand-alone peaks. A previous study defined this secondary anodic current as a potential-driven hydride transfer from the α-carbon of the alcohol moiety to the Ni^{4+} sites, resulting in the reduction of Ni^{4+} to Ni^{2+}.[22] It was further proposed that this hydride transfer pathway was more prominent in the case of HMF owing to the presence of the alcohol group, whereas the indirect oxidation pathway was the governing mechanism for DFF and FFCA. This interpretation is further substantiated by the CV results presented in this work.

3.4. Photoelectrochemical HMF oxidation

For the PEC reaction, an n-type nanoporous $BiVO_4$ photoanode prepared on a FTO substrate through a well-established synthesis method was employed as the photoanode.[29] The $Ni(OH)_2$ redox catalyst was subsequently electrodeposited onto the $BiVO_4$ substrate following the same procedure developed earlier in this study, with the only modification being the replacement of the FTO working electrode with the $BiVO_4$ electrode. This approach is based on the hypothetical premise that $Ni(OH)_2$ would uniformly coat the surface of the $BiVO_4$ nanoparticles, as obtained with FTO, while preserving its nanostructured morphology. This hypothesis was validated by examining the $BiVO_4$ electrodes using SEM (Fig. 7). Compared to the pristine $BiVO_4$ surface prior to electrodeposition (Fig. 7a), the post-deposition image (Fig. 7b) reveals ultrafine nanoparticles uniformly distributed on each $BiVO_4$ grain. The $BiVO_4$ particles acquire a visibly roughened texture relative to their original smooth surface. The morphology of the $Ni(OH)_2$ coating is herein referred to as a nanoweb structure, highlighting its consistent, porous, and conformal coverage across the surface of the $BiVO_4$ electrode.

The PEC configuration was assembled using the $Ni(OH)_2$-decorated $BiVO_4$ as the photoanode, illuminated by an AM 1.5 G light source (100 mW cm^{-2}). The proposed PEC mechanism for HMF oxidation over the $Ni(OH)_2$-modified $BiVO_4$ photoanode is illustrated in Fig. 8. Upon illumination, incident photons are absorbed by $BiVO_4$, generating electron–hole pairs that are promptly separated. The
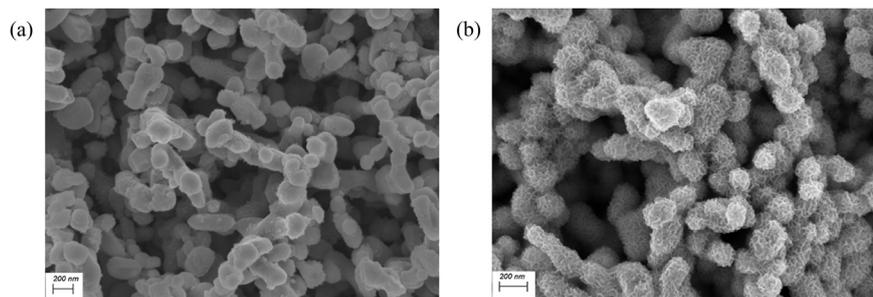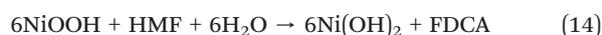
610 | *Catal. Sci. Technol.*, 2026, **16**, 602–617

This journal is © The Royal Society of Chemistry 2026

Fig. 7 SEM images of the $BiVO_4$ nanoparticles (a) before and (b) after electrodeposition of $Ni(OH)_2$ at −0.7 V vs. RHE for 15 minutes.

photogenerated holes in the valence band migrate toward the $BiVO_4$–$Ni(OH)_2$ interface, initiating the oxidation of $Ni(OH)_2$ to NiOOH (eqn (13)). The migration direction of photogenerated holes across the $BiVO_4$–$Ni(OH)_2$ junction and the sequential participation in $Ni(OH)_2$ oxidation was verified by control experiments with the introduction of 1 M Na_2SO_3 as a hole scavenger, and the corresponding results are provided in SI Fig. S6. The resulting NiOOH subsequently acts as chemical oxidant that facilitates the conversion of HMF to FDCA through sequential oxidation steps at the electrode–electrolyte interface (eqn (14)). Simultaneously, the photogenerated electrons are directed to a Pt cathode through an external circuit, where they participate in the hydrogen evolution reaction (HER) (eqn (15)). To mitigate the effect of dissolved O_2 on the desired PEC reactions, the electrolytes were purged with N_2 for 30 minutes before each measurement.

$$\text{Anode: } 6Ni(OH)_2 + 6h^+ + 6OH^- \rightarrow 6NiOOH + 6H_2O \quad (13)$$

$$6NiOOH + HMF + 6H_2O \rightarrow 6Ni(OH)_2 + FDCA \quad (14)$$

$$\text{Cathode: } 6H_2O + 6e^- \rightarrow 3H_2 + 6OH^- \quad (15)$$

LSV scans were conducted in borate buffer with and without the addition of 5 mM HMF, and the resulting

Fig. 8 Schematic illustration of the proposed photoelectrochemical mechanism for HMF oxidation on the $Ni(OH)_2$-modified $BiVO_4$ photoanode. Competing side reactions including the direct OER on the exposed $BiVO_4$ at the anode and the ORR at the cathode are shown in red.

photocurrent responses are presented in Fig. 9a. Unlike in electrochemical systems, where the applied bias directly provides the overpotential to drive the reactions, the photocurrent in PEC systems originates from the photogenerated charge carriers that participate in the reactions. Therefore, the photocurrent is only determined by the bandgap and the band-edge positions of the semiconductor photoelectrode, while the applied potential merely serves to assist the charge separation. The $BiVO_4$ photoanode employed in this study features a valence band position ($\sim$2.4 V vs. RHE)[58] that is substantially more positive than the standard potentials for either the OER (1.23 V) (eqn (16)) and $Ni(OH)_2$ oxidation (1.40 V). As a result, the photocurrent obtained in the low-potential region in the absence of HMF (black line) arises from the combined contributions of both $Ni(OH)_2$ oxidation and the competing OER occurring at the uncoated regions of the $BiVO_4$ surface, as illustrated in Fig. 8. Accordingly, the photocurrent increases steadily with increasing potential, approaching a plateau at 0.5 V vs. RHE, at which point $Ni(OH)_2$ starts depleting and the OER dominates the anodic reaction. In the absence of a membrane separator, the O_2 generated at the photoanode can dissolve into the electrolyte and can potentially diffuse toward the cathode, where it may undergo the cathodic O_2 reduction reaction (eqn (17)) owing to its more favourable thermodynamics compared to the HER. The possible occurrence of these side reactions during the PEC operation is therefore recognised.

$$4OH^- + 4h^+ \rightarrow O_2 + 2H_2O \quad (16)$$

$$O_2 + 2H_2O + 4e^+ \rightarrow 4OH^- \quad (17)$$

At applied potentials exceeding 0.9 V vs. RHE, a secondary current rise is observed, reflecting the growing influence of dark current. This suggests a transition from predominantly photo-driven processes to potential-dependent electrochemical reactions. In comparison, the introduction of 5 mM HMF leads to a distinct enhancement of photocurrent within the low potential region, corresponding to the concurrent HMF oxidation and chemical regeneration of $Ni(OH)_2$, as previously discussed. At higher applied potentials, the photocurrent difference between the presence
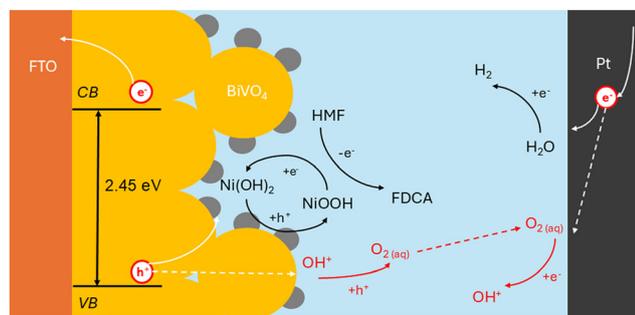
This journal is © The Royal Society of Chemistry 2026

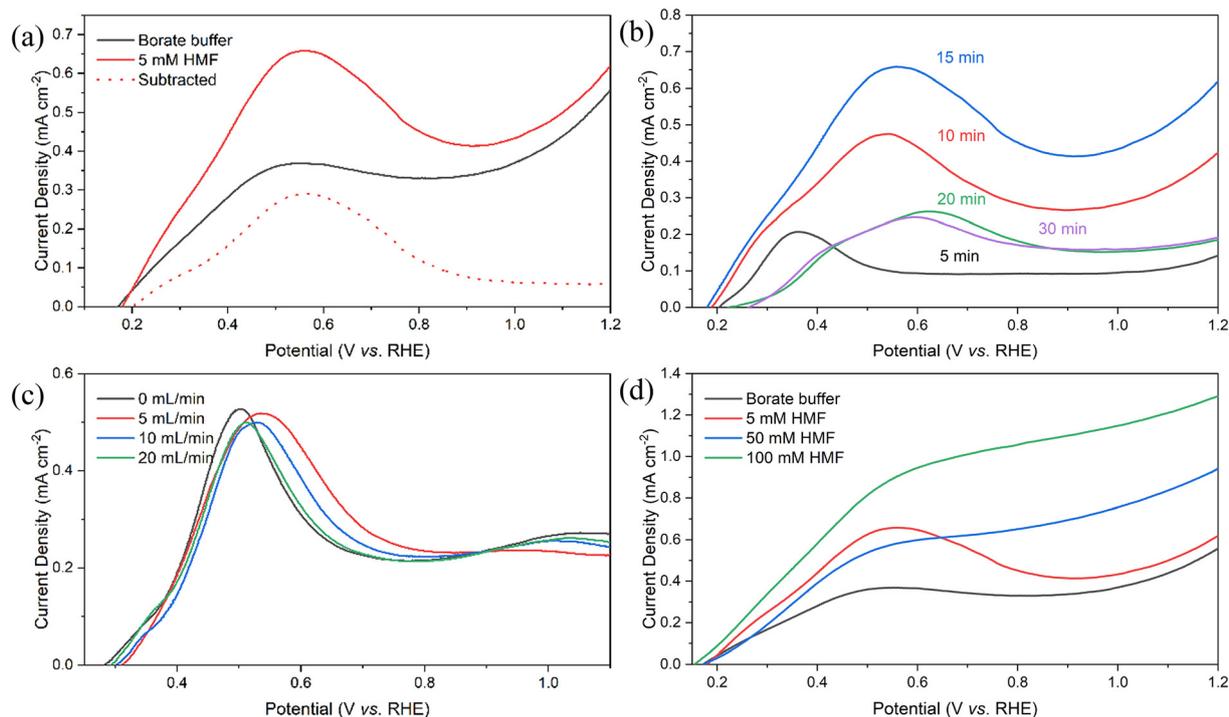Catal. Sci. Technol., 2026, **16**, 602–617 | **611**

Fig. 9 Photocurrent response of Ni(OH)$_2$-decorated BiVO$_4$ photoanodes under AM 1.5 G illumination (100 mW cm^{-2}). (a) LSV scans of a 15 minute electrodeposited electrode measured in borate buffer with (red) and without (black) 5 mM HMF. The dotted line represents the net photocurrent obtained by subtracting the baseline response in buffer alone. (b) LSV scans of BiVO$_4$ electrodes electrodeposited with Ni(OH)$_2$ for various deposition times from 5 to 30 minutes, measured in borate buffer with 5 mM HMF. (c) LSV scans in 5 mM HMF measured at different electrolyte flow rates using a laminar flow cell. (d) LSV responses recorded with varying HMF concentrations in a batch reactor with agitation. Scan rate = 10 mV s^{-1}.

and the absence of HMF diminishes and the net contribution from the HMF oxidation (with the borate buffer baseline subtracted) stabilises at approximately 0.06 mA cm^{-2}. This consistent interval indicates the sustained and steady regeneration rate of Ni(OH)$_2$ via the interfacial chemical reaction between NiOOH and HMF.

To evaluate the influence of the quantity of Ni(OH)$_2$ coating on the photocurrent response, LSV scans were performed in the 5 mM HMF solution using working electrodes prepared with varying electrodeposition times. Since the electrodeposition of Ni(OH)$_2$ proceeds via an indirect mechanism, where particle precipitation is induced by a cathodically driven pH increase, the amount of Ni(OH)$_2$ deposited does not follow a direct proportion with the charge passed during the deposition. Although the exact quantity of Ni(OH)$_2$ cannot be accurately determined using Faraday's law, a general positive correlation between the charge passed and the Ni(OH)$_2$ quantity is anticipated. For clarity and more intuitive demonstration, the amount of deposited Ni(OH)$_2$ is thus expressed in terms of deposition duration from 5 to 30 minutes. As shown in Fig. 9b, comparison of electrodes with deposition times of 5, 10, and 15 minutes reveals a clear overall trend of increasing photocurrent with extending deposition times. This is evidently due to the increased surface coverage of Ni(OH)$_2$. Notably, the photocurrent enhancement remains pronounced even following the

depletion of Ni(OH)$_2$, indicating that the quantity of the initial Ni(OH)$_2$ coating also has an effect on the PEC rate of the OER. Since the CV analyses (Fig. 6 and 8) demonstrated that the electrochemically formed NiOOH exhibits limited intrinsic catalytic activity for OER, the observed current increase is believed to result from the generation of Ni^{4+} and Ni^{6+}, driven by the sufficiently positive valence band of BiVO$_4$. These species are known to facilitate the OER, thus contributing to the overall photocurrent.

Interestingly, a significant decline in overall photocurrent is observed when the deposition time reaches 20 minutes. The reduction in dark current at a high-potential region is also evident. However, further increases in deposition time beyond 20 minutes result in only marginal decreases in current. This phenomenon is most plausibly caused by the increasing surface coverage of Ni(OH)$_2$, which leads to a blockage of the active sites. In addition, excessive accumulation of NiOOH may exacerbate the charge recombination at the BiVO$_4$–NiOOH interface, which is a known limitation in such heterojunction systems.[29] The calculated charge separation efficiencies (SI Fig. S7) reveal a clear decrease at 1.0 V vs. RHE for the Ni(OH)$_2$-coated electrode compared to pristine BiVO$_4$, confirming the intensified interfacial charge recombination effect at the Ni(OH)$_2$–BiVO$_4$ junction. Therefore, a 15 minute deposition time was adopted for all further experiments to ensure an

612 | *Catal. Sci. Technol.*, 2026, **16**, 602–617

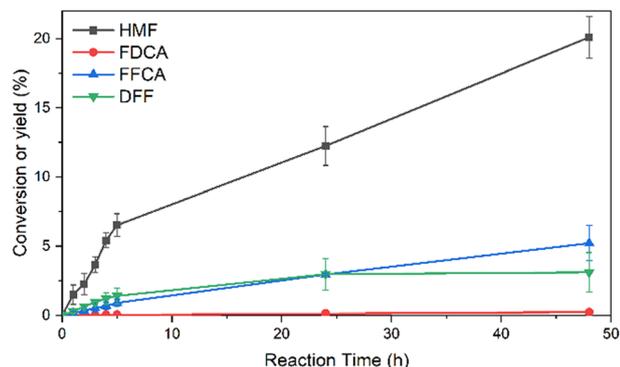This journal is © The Royal Society of Chemistry 2026

Fig. 10 Product analyses following a 48 hour PEC oxidation of 5 mM HMF using a Ni(OH)$_2$-decorated BiVO$_4$ photoanode. Error bars indicate maximum deviations across three trials.

optimal reaction rate. Furthermore, shoulder photocurrents were generally observed closely prior to the dominant peak and became increasingly pronounced with increasing electrodeposition time. This feature is attributed to the formation of multilayer Ni(OH)$_2$ particles, where the outer domains are not in direct contact with the underlying BiVO$_4$. As a result, the photogenerated holes need to travel a longer distance before reaching the electroactive Ni^{2+} species, overcoming a greater charge recombination effect. A higher electric field is therefore required to drive the charge separation, leading to delayed Ni^{2+} oxidation at the outer layer, manifested as shoulder photocurrents.

Prolonged PEC reactions were carried out on the Ni(OH)$_2$-mediated photoanode system over an extended period of 48 hours. A constant potential of 1.05 V *vs.* RHE was applied to ensure sufficient driving force for charge separation while preventing direct electrochemical oxidation reactions. HMF conversion and product yields were quantified through HPLC analysis of aliquots periodically withdrawn from the electrolyte (Fig. 10). Compared to the trace conversion observed with a pristine BiVO$_4$ photoanode, a clear HMF conversion was achieved with the Ni(OH)$_2$-coated electrode and increased as the reaction proceeded (SI Fig. S8). DFF emerged as the primary product in the early stage of the reaction and was surpassed by FFCA after 24 hours. No detectable amount of HMFCA was observed throughout the operation, consistent with the established oxidation pathway. Although the FDCA yield remained low at 0.23% after 48 hours, the formation of key intermediates, DFF and FFCA, with respective yields of 3.1% and 5.2% supports the viability of the proposed Ni-mediated oxidation mechanism. It is noted that the amount of HMF consumed was 12% more than the combination of all the quantified products, suggesting the occurrence of side reactions which produce molecules that are difficult to analytically detect and identify. Among the plausible by-products, humin, formed through polymerisation and condensation, has been frequently mentioned in the literature as a coexistent outcome of HMF oxidation.[59–62] Upon a total charge of 2.29C passed over the course of the 48 hour reaction, a total FE of only 67% was

recorded. While the presence of some Ni species that remained in their oxidised form at the time of final sampling as well as the unidentifiable oxidation by-products may account for the loss of effective FE, the relatively low value indicates that the OER, either *via* direct oxidation at the BiVO$_4$–electrolyte interface or through sequential oxidation by high-valent Ni species, plays a substantial role in the anodic PEC reactions. A control experiment without HMF confirmed that the OER is a substantial competing reaction, with 1.39C of charge passed under identical operating conditions. After excluding the first hour, during which photocurrents were presumably dominated by Ni(OH)$_2$ oxidation in both cases, the charge passed without HMF still accounted for 59% of that with HMF. Although competitive adsorption between HMF and OH$^-$ ions prevents a simple quantitative deconvolution, these results indicate that the OER accounts for a major part of the observed FE loss.

3.5. Kinetic analysis

To improve process efficiency and provide insight for rational catalyst design, it is important to gain a detailed understanding of the reaction kinetics occurring on the photoanode. In the present system, the overall reaction series proceeds through a hybrid mechanism involving both photo-induced solid-state charge transfer and subsequent chemical oxidation at the electrode–electrolyte interface. As these two steps happen in a sequential manner, the charge transfer step (CTS) and the interfacial chemical step (ICS) are conceptually decoupled to investigate the rate-limiting step and elucidate the governing kinetic regime.

Three potential rate-limiting factors are identified in the overall PEC process: the kinetics of the CTS, the kinetics of the ICS, and the mass transfer associated with the ICS. To determine the dominant rate-limiting step, controlled experiments were conducted by systematically varying the flow rate and substrate concentration. To first assess the role of convective mass transfer, the flow rate of the HMF-containing electrolyte was varied in a custom-designed laminar flow cell while maintaining constant illumination and substrate concentration. Since the flow cell features different dimensions, such as the electrolyte chamber volume, electrode sizes, and interelectrode spacing, the photocurrents obtained under flow conditions are not directly comparable to those measured in the batch reactor. As shown in Fig. 9c, by varying the volumetric flow rate from static to 20 mL min^{-1}, the resulting photocurrent exhibited minimal variation across the tested range, indicating that mass transfer from the bulk solution to the electrode surface is not the rate-limiting factor under these conditions. In fact, a slight positive shift in the potential required when laminar flow was induced and a reduction in photocurrent with increasing flow rate were observed. This is hypothetically due to the disruption of surface adsorption equilibria between HMF and NiOOH active sites, which controls the ICS kinetics. Although further investigation, such as through rotating disk

This journal is © The Royal Society of Chemistry 2026

Catal. Sci. Technol., 2026, **16**, 602–617 | 613

electrode or electrochemical impedance spectroscopy, is needed to validate this hypothesis, it can be reasonably concluded that the overall reaction rate is limited by the kinetics of either the CTS or the ICS instead of the mass transfer from the bulk solution to the electrode surface.

The influence of substrate concentration on the reaction kinetics was assessed by varying the HMF concentration in the bulk electrolyte from 5 mM to 100 mM under otherwise consistent conditions (Fig. 9d). Due to the slow kinetics of the initial HMF oxidation step, the rest of the consecutive steps are deemed to be negligible, and the ICS is considered to be dominated solely by HMF oxidation. Comparing the photocurrent response when increasing the concentration from 5 mM to 50 mM, a moderate decrease in photocurrent was surprisingly depicted in the low-potential region. This seemingly indicates that higher substrate concentration may counterintuitively hinder the PEC process. However, an apparent drop in photocurrent at low potentials is more likely attributed to the suppression of the OER due to the competitive adsorption between HMF and OH^- ions at the photoanode interface. The photocurrent in the high-potential region, where $Ni(OH)_2$ is depleted, is a closer representative of the steady-state kinetics of HMF oxidation, which clearly exhibited an enhancement with increased HMF concentration. Similar results were concluded upon further increasing the substrate concentration to 100 mM. When analysing the net current induced by HMF (*i.e.*, after subtracting the buffer baseline), the current established in the high-potential region appears to scale nearly proportionally with HMF concentration. This trend suggests that the interfacial HMF oxidation follows pseudo-first-order kinetics with respect to HMF, in agreement with assumptions commonly adopted in the literature.[17,63,64] HMF conversions were monitored over the PEC operations *via* HPLC at different initial concentrations, and the resulting linear $\ln(C_t/C_0)$ *vs. t* plots (SI Fig. S9) further support the pseudo-first-order behaviour of the reaction. Accordingly, the overall interfacial reaction rate can be expressed as follows:

$$r = k \cdot \theta_{\text{NiOOH}} \cdot [\text{HMF}]_s \quad (18)$$

where k is the reaction rate constant of the interfacial reaction, θ_{NiOOH} is the fractional surface coverage of active NiOOH sites, and $[\text{HMF}]_s$ is the surface concentration of HMF, which is approximately equal to $[\text{HMF}]_b$ when the mass flux to the surface is significantly faster than the rate of consumption (eqn (19)).

$$[\text{HMF}]_s = \left(1 + \frac{k}{k_m}\right)[\text{HMF}]_b \quad (19)$$

where the mass transfer coefficient, k_m, is much greater than the reaction rate constant $(k_m \gg k)$. The monotonic dependence of the reaction rate on substrate concentration discloses that the kinetics is limited by the ICS. The photogenerated holes should always be in excess to supply

the CTS within the tested range of substrate concentration. Thus, θ_{NiOOH} is considered constant and the rate expression can be simplified to eqn (20), where k' represents a rearranged kinetic constant.

$$r = k' \cdot [\text{HMF}]_b \quad (20)$$

To quantify the kinetic barrier associated with the rate-limiting ICS, temperature-dependent PEC analyses were conducted over an operating range from 25 to 55 °C. The temperature was externally controlled in an electrolyte reservoir before entering the laminar flow chamber at a constant flow rate of 5 mL min^{-1}. To ensure that mass transfer did not become the rate-limiting step at elevated temperatures, additional experiments were performed by increasing the flow rate, which produced no further photocurrent enhancement. Average current densities were recorded under potentiostatic conditions after allowing sufficient duration for steady-state operation, thereby better reflecting the intrinsic kinetics of the ICS. The monitored current densities can be seen in SI Fig. S10. A general increasing trend in photocurrent density was manifested with elevating temperature, suggesting that the overall reaction rate is thermally active. The steady-state current densities (j) are directly proportional to the rate of the ICS according to Faraday's law. As a potential-independent chemical reaction, the temperature dependence of the ICS can be described by the Arrhenius equation (eqn (21)). The logarithm plot is shown in SI Fig. S11.

$$j = nFA \cdot \exp\left(-\frac{E_a}{RT}\right) \cdot [\text{HMF}]_b \quad (21)$$

From the slope of the Arrhenius plot, an activation energy of 17.2 kJ mol^{-1} was extracted, which corresponds to the energy barrier for the chemical reaction between NiOOH and HMF at the photoanode surface. Existing kinetic studies of HMF oxidation in the literature primarily focus on thermocatalytic processes involving the use of noble metal catalysts at elevated temperatures, where activation energies typically range from 29 to 77 kJ mol^{-1}.[65,66] The lower activation energy reported in this study highlights that the NiOOH-mediated reaction proceeds with a comparatively modest energy requirement, enabling HMF oxidation under ambient conditions. However, the relatively slow kinetics may result from the limited availability of active sties on NiOOH, which in turn affect chemisorption.[21] Further enhancement of the performance of the NiOOH-mediated system could be achieved by engineering the electrodeposition process to optimise other structural properties such as the aggregation array,[24] which, along with particle size and morphology,[67] is evident to have an impact on their catalytic activity for HMF oxidation.

3.6. Long-term stability of the heterostructured photoelectrode

The crystal structure mismatch and density variation between $Ni(OH)_2$ and NiOOH are widely considered

614 | *Catal. Sci. Technol.*, 2026, **16**, 602–617

This journal is © The Royal Society of Chemistry 2026

responsible for the instability during electrocatalytic application,[68,69] as the phase transition is usually accompanied by a volume change that may lead to structural collapse over time.[23] The consistent current density observed in the aforementioned CV and *in situ* UV-vis analyses (Fig. 6b) reveals the high stability of the electrodeposited $Ni(OH)_2/NiOOH$ couple during cyclic transformation over 20 CV cycles. To further evaluate its resistance to chemical dissolution and catalyst poisoning under continuous PEC operation, the photoanode was recovered and examined after a 48 hour reaction. The electrolyte temperature was raised to 55 °C and delivered through the flow cell at 5 mL min^{-1} in order to accelerate the reaction kinetics and also assess the mechanical and thermal stability of the catalyst film. A stable current density was established after 5 hours of operation and remained steady throughout the operation. Hence, the reaction is expected to continue in a comparable rate if extended for an even longer duration. The total charge passed reached 6.02C at the time the reaction was actively ceased after 48 hours.

Post-reaction SEM imaging taken on the recovered photoanode confirms that the electrode retains excellent morphological consistency when compared to the pre-reaction state (SI Fig. S12). The LSV measured in freshly prepared 5 mM HMF electrolyte shows no substantial deterioration compared to the LSV collected prior to the reaction (SI Fig. S13). Instead, a slight negative potential shift suggests that the very subtle surface reconstruction may, in fact, be benign to the catalytic performance of NiOOH. In addition, photocorrosion of $BiVO_4$ due to interfacial charge accumulation during extended operation is a well-recognised limitation in PEC systems.[70] The $Ni(OH)_2$ coating developed in this study not only exhibits structural and electrochemical stability but also mitigates the degradation of the underlying $BiVO_4$ substrate. This highlights the dual functionality of $Ni(OH)_2$ as both a redox mediator and a protective layer for the photoanode, which reduces direct contact with the electrolyte and helps bypass the accumulation of the photogenerated holes.[71]

Building on the observation of this protective effect, a preliminary PEC experiment was performed by adjusting the electrolyte pH to 13 through the addition of NaOH to evaluate the stability of the photoanode under strongly alkaline conditions, which are widely reported to enhance the kinetics of HMF oxidation.[72,73] The results, shown in SI Fig. S14 and discussed subsequently, provide early evidence that the $Ni(OH)_2$ overlayer offers partial protection against alkaline etching while also revealing the challenges associated with $BiVO_4$ deactivation and HMF degradation under strongly alkaline conditions. Future optimisation of the protective overlayer during the electrodeposition and the reaction environment could enable PEC operation under more alkaline conditions, offering opportunities to improve both reaction kinetics and product selectivity.

4. Conclusion

In summary, this study demonstrates the effectiveness of the electrodeposited $Ni(OH)_2$ nanoparticles as a solid-state redox mediator for the PEC oxidation of HMF by forming a heterostructured photoanode with $BiVO_4$. $Ni(OH)_2$ is locally oxidised to NiOOH by the photogenerated holes and subsequently oxidises HMF and regenerates $Ni(OH)_2$. After 48 hours of PEC operation, HMF was successfully converted to FDCA, albeit with a modest yield (0.23%) and Faradaic efficiency (67%), with the majority of products comprising partially oxidised intermediates (8.3%). Kinetic studies identified that the overall reaction rate is limited by the interfacial chemical step between NiOOH and the surface-absorbed HMF, with the apparent activation energy determined to be only 17.2 kJ mol^{-1}, notably lower than those typically reported for thermocatalytic HMF oxidation. The heterostructured photoanode also maintained stable performance after extended operation under flow and elevated temperature conditions, highlighting the dual functionality of $Ni(OH)_2$ as both a redox mediator and a protective layer that mitigates photocorrosion of $BiVO_4$. Notably, a near-neutral pH was selected to ensure the long-term stability of the $BiVO_4$ photoanode. Owing to the protective functionality of the $Ni(OH)_2$ overlayer, future investigations may focus on optimising operating conditions in more alkaline environments, where electrocatalytic FDCA production is well established, in order to further enhance the product yield and selectivity. Further performance improvements in the NiOOH-mediated system could also be achieved by engineering the electrodeposition process to optimise the particle properties of $Ni(OH)_2$, which is believed to have a significant influence on the catalytic activity toward HMF oxidation.

Author contributions

Yuming Zhang: writing – original draft, conceptualisation, methodology, formal analysis, investigation, and visualisation. Klaus Hellgardt: writing – review & editing, validation, supervision, resources, and project management.

Conflicts of interest

There are no conflicts to declare.

Data availability

The data supporting the findings of this study are included in the main text and supplementary information (SI). Supplementary information is available. See DOI: https://doi.org/10.1039/d5cy01024a.

References

1 H. G. Cha and K. S. Choi, *Nat. Chem.*, 2015, **7**, 328–333.
2 C. R. Lhermitte and K. Sivula, *ACS Catal.*, 2019, **9**, 2007–2017.

This journal is © The Royal Society of Chemistry 2026

Catal. Sci. Technol., 2026, **16**, 602–617 | **615**

3 Y. Choi, R. Mehrotra, S. H. Lee, T. V. T. Nguyen, I. Lee, J. Kim, H. Y. Yang, H. Oh, H. Kim, J. W. Lee, Y. H. Kim, S. Y. Jang, J. W. Jang and J. Ryu, *Nat. Commun.*, 2022, **13**, 5709.

4 Y. Miao and M. Shao, *Chin. J. Catal.*, 2022, **43**, 595–610.

5 X. Yue and Y. Queneau, *ChemSusChem*, 2022, **15**, e202102660.

6 Z. Z. Meng, S. S. Chen, H. R. Li and L. N. He, *ChemCatChem*, 2025, **17**, e202401658.

7 Z. Li, Y. Han, B. Huang, Z. Xie and Q. H. Wei, *Mater. Adv.*, 2023, **4**, 2449–2456.

8 J. Song, C. Wei, Z. F. Huang, C. Liu, L. Zeng, X. Wang and Z. J. Xu, *Chem. Soc. Rev.*, 2020, **49**, 2196–2214.

9 D. J. Chadderdon, L. P. Wu, Z. A. McGraw, M. Panthani and W. Li, *ChemElectroChem*, 2019, **6**, 3387–3392.

10 L. Zheng, P. Xu, Y. Zhao, Z. Bao, X. Luo, X. Shi, Q. Wu and H. Zheng, *Appl. Catal., B*, 2023, **331**, 122679.

11 I. Carrai, R. Mazzaro, E. Bassan, G. Morselli, A. Piccioni, S. Grandi, S. Caramori, P. Ceroni and L. Pasquini, *Sol. RRL*, 2023, **7**, 2300205.

12 A. Kawde, M. Sayed, Q. Shi, J. Uhlig, T. Pullerits and R. Hatti-Kaul, *Catalysts*, 2021, **11**, 969.

13 J. Xiao, C. Li, X. Jia, J. Sun, F. Liubov, C. Liang, X. Zhang and B. Wang, *Electrochim. Acta*, 2024, **475**.

14 I. Carrai, R. Mazzaro, C. Bellatreccia, A. Piccioni, M. Salvi, S. Grandi, S. Caramori, P. Ceroni and L. Pasquini, *ChemSusChem*, 2025, **18**, e202402604.

15 X. Guo, J.-E. Seo, S. M. Bryce, J. A. Tan, Q. Wu, S. L. Dial, M. M. Moore and N. Mei, *Toxicol. Sci.*, 2018, 214–225.

16 X. Guo, R. A. Mittelstaedt, L. Guo, J. G. Shaddock, R. H. Heflich, A. H. Bigger, M. M. Moore and N. Mei, *Toxicol. In Vitro*, 2013, **27**, 1496–1502.

17 C. R. Lhermitte, N. Plainpan, P. Canjura, F. Boudoire and K. Sivula, *RSC Adv.*, 2020, **11**, 198–202.

18 K. R. Vuyyuru and P. Strasser, *Catal. Today*, 2012, **195**, 144–154.

19 G. R. Xu, M. Batmunkh, S. Donne, H. Jin, J. X. Jiang, Y. Chen and T. Ma, *J. Mater. Chem. A*, 2019, **7**, 25433–25440.

20 D. J. Chadderdon, L. Xin, J. Qi, Y. Qiu, P. Krishna, K. L. More and W. Li, *Green Chem.*, 2014, **16**, 3778–3786.

21 R. Luo, Y. Li, L. Xing, N. Wang, R. Zhong, Z. Qian, C. Du, G. Yin, Y. Wang and L. Du, *Appl. Catal., B*, 2022, **311**, 121357.

22 M. T. Bender and K. S. Choi, *ChemSusChem*, 2022, **15**, e202200675.

23 Y. Huang, X. Pang, J. Cui, Z. Huang, G. Wang, H. Zhao, H. Bai and W. Fan, *Inorg. Chem.*, 2023, **62**, 6499–6509.

24 J. Wang, W. Zhao, H. Yu, W. Wang, Y. Xu, L. L. Shen, G. R. Zhang and D. Mei, *Appl. Catal., B*, 2024, **353**, 124086.

25 M. T. Bender, R. E. Warburton, S. Hammes-Schiffer and K. S. Choi, *ACS Catal.*, 2021, **11**, 15110–15124.

26 K. Juodkazis, J. Juodkazytė, R. Vilkauskaitė and V. Jasulaitienė, *J. Solid State Electrochem.*, 2008, **12**, 1469–1479.

27 K. Zhang, J. H. Park, J. Liu, L. Wang, B. Jin, X. Yang and S. Zhang, *J. Am. Chem. Soc.*, 2020, **142**, 8641–8648.

28 Y. An, X. Yang, R. Wang, Y. Gu, Y. Min, T. Zhang, J. Shen and K. Zhang, *Angew. Chem., Int. Ed.*, 2025, e202518020.

29 T. W. Kim and K. S. Choi, *Science*, 2014, **343**, 990–994.

30 S. Zhang, I. Ahmet, S.-H. Kim, O. Kasian, A. M. Mingers, P. Schnell, M. Kölbach, J. Lim, A. Fischer, K. J. J. Mayrhofer, S. Cherevko, B. Gault, R. van de Krol, C. Scheu, S. Zhang, S. Kim, O. Kasian, A. M. Mingers, J. Lim, B. Gault, C. Scheu, I. Ahmet, P. Schnell, M. Kölbach, R. van de Krol, A. Fischer, K. J. J. Mayrhofer and S. Cherevko, *ACS Appl. Energy Mater.*, 2020, **3**(10), 9523–9527.

31 Y. Lu, T. Liu, C. L. Dong, C. Yang, L. Zhou, Y. C. Huang, Y. Li, B. Zhou, Y. Zou and S. Wang, *Adv. Mater.*, 2022, **34**, 2107185.

32 D. Wang, P. Wang, S. Wang, Y. H. Chen, H. Zhang and A. Lei, *Nat. Commun.*, 2019, **10**, 2796.

33 T. Noël, Y. Cao and G. Laudadio, *Acc. Chem. Res.*, 2019, **52**, 2858–2869.

34 M. A. Modestino, S. M. H. Hashemi and S. Haussener, *Energy Environ. Sci.*, 2016, **9**, 1533–1551.

35 I. Holmes-Gentle, F. Hoffmann, C. A. Mesa and K. Hellgardt, *Sustainable Energy Fuels*, 2017, **1**, 1184–1198.

36 Y. Yang and T. Mu, *Green Chem.*, 2021, **23**, 4228–4254.

37 X. Jiang, W. Li, Y. Liu, L. Zhao, Z. Chen, L. Zhang, Y. Zhang and S. Yun, *SusMat*, 2023, **3**, 21–43.

38 O. Nolte, P. Rohland, N. Ueberschaar, M. D. Hager and U. S. Schubert, *J. Power Sources*, 2022, **525**, 230996.

39 E. Falbo, M. Fusè, F. Lazzari, G. Mancini and V. Barone, *J. Chem. Theory Comput.*, 2022, **18**, 6203–6216.

40 J. B. Gerken and S. S. Stahl, *ACS Cent. Sci.*, 2015, **1**, 234–243.

41 D. Di Girolamo, M. Piccinni, F. Matteocci, A. G. Marrani, R. Zanoni and D. Dini, *Electrochim. Acta*, 2019, **319**, 175–184.

42 J. Desilvestro, D. A. Corrigon and M. J. Weaver, *J. Electrochem. Soc.*, 1988, **135**, 885.

43 D. Kang, T. W. Kim, S. R. Kubota, A. C. Cardiel, H. G. Cha and K. S. Choi, *Chem. Rev.*, 2015, **115**, 12839–12887.

44 Y. M. Wang, D. D. Zhao, Y. Q. Zhao, C. L. Xu and H. L. Li, *RSC Adv.*, 2012, **2**, 1074–1082.

45 M. Wohlfahrt-Mehrens, R. Oesten, P. Wilde and R. A. Huggins, *Solid State Ionics*, 1996, **86**, 841–847.

46 Y. Xin, X. Dai, G. Lv, X. Wei, S. Li, Z. Li, T. Xue, M. Shi, K. Zou, Y. Chen and Y. Liu, *ACS Appl. Mater. Interfaces*, 2021, **13**, 28118–28128.

47 T. H. Wu and B. W. Hou, *Catal. Sci. Technol.*, 2021, **11**, 4294–4300.

48 J. Yao, R. Huang, J. Jiang, S. Xiao and Y. Li, *International Journal of Ionics*, 2021, **27**, 1125–1135.

49 X. Li, K. Patil, A. Agarwal, P. Babar, J. S. Jang, X. Chen, Y. T. Yoo and J. H. Kim, *New J. Chem.*, 2022, **46**, 2044–2052.

50 J. Gallenberger, H. Moreno Fernández, A. Alkemper, M. Li, C. Tian, B. Kaiser and J. P. Hofmann, *Catal. Sci. Technol.*, 2023, **13**, 4693–4700.

51 H. Liu, Z. Yan, X. Chen, J. Li, L. Zhang, F. Liu, G. Fan and F. Cheng, *Research*, 2020, **2020**, 9068270.

52 Q. He, Y. Wan, H. Jiang, Z. Pan, C. Wu, M. Wang, X. Wu, B. Ye, P. M. Ajayan and L. Song, *ACS Energy Lett.*, 2018, **3**, 1373–1380.

53 L. Trotochaud, S. L. Young, J. K. Ranney and S. W. Boettcher, *J. Am. Chem. Soc.*, 2014, **136**, 6744–6753.

616 | *Catal. Sci. Technol.*, 2026, **16**, 602–617

This journal is © The Royal Society of Chemistry 2026

54 A. Mavrič, M. Fanetti, Y. Lin, M. Valant and C. Cui, *ACS Catal.*, 2020, **10**, 9451–9457.

55 M. C. Biesinger, L. W. M. Lau, A. R. Gerson and R. S. C. Smart, *Phys. Chem. Chem. Phys.*, 2012, **14**, 2434–2442.

56 E. L. Ratcliff, J. Meyer, K. X. Steirer, A. Garcia, J. J. Berry, D. S. Ginley, D. C. Olson, A. Kahn and N. R. Armstrong, *Chem. Mater.*, 2011, **23**, 4988–5000.

57 B. P. Payne, M. C. Biesinger and N. S. McIntyre, *J. Electron Spectrosc. Relat. Phenom.*, 2009, **175**, 55–65.

58 Y. Park, K. J. Mc Donald and K. S. Choi, *Chem. Soc. Rev.*, 2013, **42**, 2321–2337.

59 M. Kim, Y. Su, A. Fukuoka, E. J. M. Hensen and K. Nakajima, *Angew. Chem.*, 2018, **130**, 8367–8371.

60 J. C. Velasco Calderón, J. S. Arora and S. H. Mushrif, *ACS Omega*, 2022, **7**, 44786–44795.

61 L. Gálvez-Vázquez, A. Dutta, S. Vesztergom, Z. Szakály, R. Zaugg, A. V. Rudnev and P. Broekmann, *J. Catal.*, 2025, **450**, 116321.

62 M. L. Krebs, A. Bodach, C. Wang and F. Schüth, *Green Chem.*, 2023, **25**, 1797–1802.

63 C. R. Lhermitte, J. Garret Verwer and B. M. Bartlett, *J. Mater. Chem. A*, 2016, **4**, 2960–2968.

64 X. Chen, H. Li, Y. Lu, Z. Liu, Z. Ma and Y. Zhang, *ACS Sustainable Chem. Eng.*, 2025, 4242–4251.

65 S. E. Davis, A. D. Benavidez, R. W. Gosselink, J. H. Bitter, K. P. De Jong, A. K. Datye and R. J. Davis, *J. Mol. Catal. A: Chem.*, 2014, **388–389**, 123–132.

66 Z. Yuan, B. Liu, P. Zhou, Z. Zhang and Q. Chi, *Catal. Sci. Technol.*, 2018, **8**, 4430–4439.

67 P. Zhou, X. Lv, S. Tao, J. Wu, H. Wang, X. Wei, T. Wang, B. Zhou, Y. Lu, T. Frauenheim, X. Fu, S. Wang and Y. Zou, *Adv. Mater.*, 2022, **34**, 2204089.

68 S. Dai, Z. Zhang, J. Xu, W. Shen, Q. Zhang, X. Yang, T. Xu, D. Dang, H. Hu, B. Zhao, Y. Wang, C. Qu, J. Fu, X. Li, C. Hu and M. Liu, *Nano Energy*, 2019, **64**, 103919.

69 J. Wang, J. Li, Y. Liu, M. Wang and H. Cui, *J. Mater. Sci.*, 2021, **56**, 3011–3023.

70 D. K. Lee and K. S. Choi, *Nat. Energy*, 2018, **3**, 53–60.

71 T. W. Kim and K. S. Choi, *J. Phys. Chem. Lett.*, 2016, **7**, 447–451.

72 X. Liu, R. Wang, M. Wei, X. Wang, J. Qiu, J. Zhang, S. Li and Y. Chen, *J. Colloid Interface Sci.*, 2024, **657**, 438–448.

73 L. Guo, X. Zhang, L. Gan, L. Pan, C. Shi, Z. Huang, X. Zhang and J. Zou, *Adv. Sci.*, 2023, **10**, 2205540.

This journal is © The Royal Society of Chemistry 2026

Catal. Sci. Technol., 2026, **16**, 602–617 | **617**